

Enhanced Image Reconstruction in Electrical Impedance Tomography using Radial Basis Function Neural Networks

Serge Ayme Kouakouo Nomvussi*, Jan Mikulka

Department of Theoretical and Experimental Electrical Engineering, Brno University of Technology, Antonínská 548/1, 60190, Brno, Czech Republic, 244245@vut.cz, mikulka@vut.cz.

Abstract: This paper presents a novel cascade algorithm for image reconstruction in electrical impedance tomography (EIT) using radial basis function neural networks. The first subnetwork applies a density-based algorithm and k-nearest neighbors (KNN) to determine the center and width of the radial basis function neural networks, with the aim of preventing ill-conditioned connection weights between the hidden and output layers. The second subnetwork is a generalized regression neural network dedicated to functional approximation. The combined subnetworks result in a reduced mean square error and achieve an accuracy of 89.54 % without noise and an accuracy between 82.90 % and 89.53 % with noise levels ranging from 30 to 60 dB. In comparison, the original radial basis function neural networks (RBFNN) method achieves an accuracy of 85.44 % without noise and between 80.90 % and 85.31 % under similar noise conditions. The total variation (TV) method achieves 83.13 % without noise, with noise-influenced accuracy ranging from 34.28 % to 45.15 %. The Gauss-Newton method achieves 82.35 % accuracy without noise, with accuracy ranging from 33.21 % to 46.15 % in the presence of noise. The proposed method proves to be resilient to various types of noise, including white Gaussian noise, impulsive noise, and contact noise, and consistently delivers superior performance. It also outperforms the other methods in noise-free conditions. The reliability of the method in noisy environments supports its potential application in the development of new modular systems for electrical impedance tomography.

Keywords: Artificial neural network, density-based algorithm, electrical impedance tomography, k-nearest neighbors, radial basis function neural networks, EIDORS framework.

1. INTRODUCTION

Electrical impedance tomography (EIT) is a versatile, non-invasive imaging technique with many applications. It reconstructs the conductivity distributions within objects by measuring the electrical impedance on their surfaces and offers advantages such as radiation-free operation, cost-effectiveness, portability, and real-time imaging. The versatile diagnostic and imaging solutions provided by EIT show great promise in various fields, such as medicine (lung ventilation and breast cancer detection) [1], [2], industry (process monitoring and material testing) [3], and geophysics (subsurface investigations) [4]. These advantages inspire researchers and professionals to explore and innovate in this exciting field.

The main components of EIT include electrodes, acquisition electronics [5], and monitoring units. A low-intensity alternating current is introduced via electrode pairs, and the potential differences across the other electrodes are measured. These boundary voltages are crucial for the reconstruction of the conductivity maps. However, this process is inherently challenging. Various algorithms have been used to address this issue. Although non-iterative

methods are simple, they require higher accuracy due to linear approximations. On the other hand, iterative algorithms, while powerful, are susceptible to noise and measurement errors, emphasizing the need for precision in the EIT process [6]. Artificial neural networks (ANNs), especially deep Neural Networks (DNNs) with multilayer autoencoders [7], [8], have been shown to be superior in image reconstruction compared to traditional methods. Their practical applications in identifying complex patterns are particularly inspiring. Convolutional Neural Networks (CNNs) are used in noisy scenarios [9], [10], [11] and provide a practical solution for filtering noisy input data. Radial basis function neural networks (RBFNNs) approximate nonlinear functions and are enhanced by optimization algorithms such as hybrid particle swarm optimization (HPSO) [6]. They provide practical solutions for cases where the input and output data relationship is nonlinear and complex. Additionally, the RBFNN optimized by a colony of artificial bees (ABC-RBFNN) [12] and the mechanism combining the RBFNN and CBAM-UNet subnetworks further improve image quality and edge sharpness [13], inspiring further practical applications in this field.

Despite the considerable promise of EIT, persistent challenges undermine its effectiveness, particularly in the accurate reconstruction of conductivity maps from boundary voltage measurements. A persistent obstacle lies in the ill-conditioned connection weights within RBFNNs, which significantly impact prediction accuracy and image quality. There is an urgent need to revise traditional approaches to parameter determination in RBFNNs, which often rely on fixed-width and center parameters or on methods such as k-nearest neighbors (KNN) and k-means clustering [6], [14]. The KNN method requires prior knowledge of the number of clusters and risks compromising accuracy. This study presents a novel algorithmic paradigm leveraging density-based clustering algorithms (DBSCAN) [15], which dynamically adapt to different data densities without predefining cluster counts. By integrating DBSCAN into the parameter determination process, our proposed approach aims to circumvent the challenges posed by ill-conditioned weights in RBFNNs, thereby improving prediction accuracy and image quality in various EIT applications. This work complements the ongoing research work of the Department of Theoretical and Experimental Electrical Engineering to develop a new modular system [16] for EIT.

While previous studies have mainly relied on datasets with constant-conductivity objects and white Gaussian noise, our research takes a different approach. We use a synthetic dataset generated using the EIDORS framework [17], a widely used software package for EIT, containing objects with different shapes (rectangular and circular) and distinct conductivities. We designed this dataset to mimic real-world scenarios, adding a layer of complexity to the research. Furthermore, our study extends its scope to include white Gaussian noise and non-Gaussian noise sources such as impulsive and contact noise. This departure from conventional constant conductivity targets and noise sources enriches our research with a more realistic and complex dataset, adding depth and nuance to our EIT investigations and covering a wider range of real-world noise scenarios. Using the EIDORS framework and including different noise sources in our dataset are crucial aspects of our research, as they allow us to simulate and study EIT in a more realistic and challenging environment, improving the robustness and applicability of our proposed algorithmic paradigm. Our work has practical implications as it provides a more accurate and comprehensive understanding of EIT under real-world conditions.

2. MATERIALS AND METHODS

In our study on the reconstruction of EIT images using ANNs, the dataset acquisition phase was of central importance. To this end, we generated a synthetic dataset using the well-established EIDORS framework. We chose EIDORS in our methodology for dataset creation because it effectively solves forward and inverse EIT problems and is highly practical. EIDORS enabled the generation of a diverse dataset with circular and rectangular targets with different conductivity levels and sizes in a water-filled vessel. The choice of a constant water conductivity of 0.04 S/m and an object conductivity ranging from 0.01 S/m to 0.12 S/m is significant as it represents a realistic range of conductivities

in typical EIT applications. We chose these conductivity levels to mimic the range of conductivities in biological tissue so that our dataset is more representative of real-world scenarios. We use electrodes surrounding the container to inject current and measure the voltage, as shown in Fig. 1, following predetermined patterns. The container has a diameter of 100 mm. To adapt the newly proposed technique for different EIT applications, several key parameters need to be considered. The frequency of current injection, which ranges from 10 kHz to 200 kHz, should be adjusted based on the specific properties of the target medium, as different frequencies offer different sensitivity to conductivity changes. Higher frequencies often provide better resolution for fine structures. The number of electrodes, which is fixed at 16 in the current setup, may need to be adjusted depending on the spatial resolution requirements of the application. This is a crucial factor that emphasizes the significance of your role, as potential modifications can lead to higher accuracy or coverage if needed. In addition, the current injection and measurement patterns should be tailored to the specific imaging task to optimize sensitivity and image reconstruction quality.

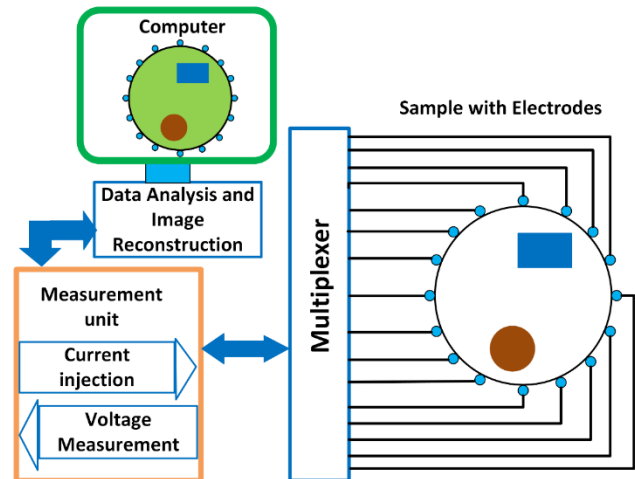


Fig. 1. EIT system with electrodes.

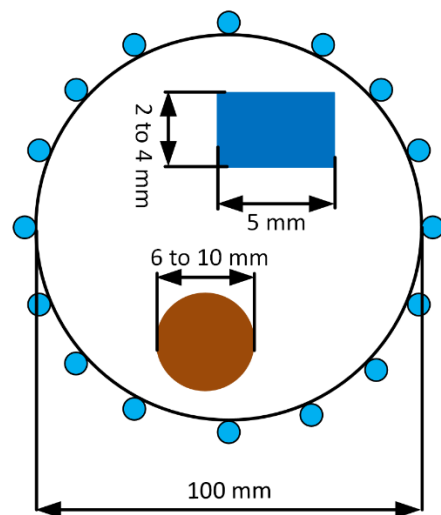


Fig. 2. Vessel and object size.

In comparison, the circular targets have a diameter of 6 to 10 mm, and the rectangular targets measure 5 mm in length and 2 to 5 mm in width, as shown in Fig. 2. This meticulous setup ensures a comprehensive dataset that is not only diverse but also representative of real-world scenarios. While we recognize the maturity of the EIDORS system, its integration into our methodology served a very specific purpose: to facilitate robust dataset preparation and allow us to focus on algorithm development and evaluation. Although the use of EIDORS is not a new aspect, its pragmatic incorporation underlines our methodological efficiency and research orientation.

Our study explores two distinct injection and voltage measurement patterns: adjacent injection and measurement and another in which two electrodes separate the injection and measurement phases.

The finite element model (FEM) integrated into the EIDORS framework is based on a homogeneous cylindrical object known as d2c, comprising 1024 pixels configured in a 16-electrode pattern. Each dataset sample can have circular, rectangular, or both shapes for training, testing, and validation. The measured voltage and conductivity maps serve as input and output data for the novel RBFNN, respectively. The input voltage ranges from 0.43 to 28.26 mV, while the conductivity values in the reconstructed images vary between 0.04 and 0.29 S/m. The input vector U_i comprises 208 measured voltages, while the output vector σ comprises 1024 conductivity values, as detailed in (1) and (2).

Regarding dataset sizes, it is essential to note that the extensive dataset comprises 10647 samples in the training dataset and 3561 samples each in the validation and test datasets. While the numbers 10647 and 3561 have no particular significance beyond indicating the scale of the dataset, they do indicate the sample sizes in each partition. This clarification ensures transparency regarding the composition and distribution of the dataset and provides a comprehensive overview of our experimental setup.

It is important to emphasize that noise was intentionally

introduced during the voltage measurement process to replicate real-world scenarios. This noise, with a typical signal-to-noise ratio (SNR) between 30 and 60 dB, includes both white Gaussian noise and non-Gaussian noise sources, such as impulsive and contact noise. It is important to note that contact noise is caused by poor contact between the electrode and the skin or by the electrode movement. This noise leads to electrode impedance variations that significantly affect the signal quality. The deliberate inclusion of different types of noise reinforces the robustness of the ANN model and guarantees its effectiveness in practice in noisy environments.

Fig. 3 shows the process of generating and using synthetic data for training ANNs. The process begins with a known current I and an initial conductivity σ_{before} before solving the forward problem. The electrical distribution ϕ is then determined, which is then used to measure the boundary voltage U_i . The final step is to solve the inverse problem to reconstruct the sample conductivity maps σ after. This process is not a one-time event, but an iterative process that is repeated through numerous simulations to generate a substantial dataset. The boundary voltages and the initial conductivity σ_{before} serve as input and output parameters for the new method. Different types of noise are intentionally introduced into the boundary voltage U_i to serve as input for the ANN during model training.

$$U = (U_1, U_2, \dots, U_i) \quad \text{with } i = 1, 2, \dots, 128, \quad (1)$$

$$\sigma = (\sigma_1, \sigma_2, \dots, \sigma_j) \quad \text{with } j = 1, 2, \dots, 1024. \quad (2)$$

The SNR of the different noises is determined using the following equation:

$$SNR = 20 \log_{10} \left(\frac{U}{V_n} \right), \quad (3)$$

where U is the boundary voltage without noise and V_n is the noise voltage.

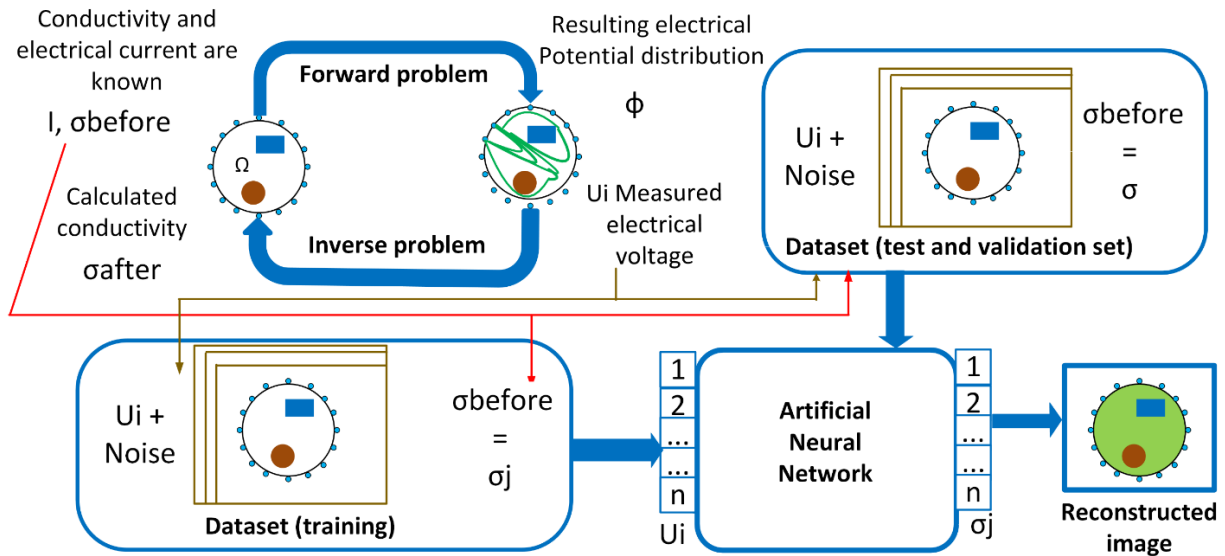


Fig. 3. Synthetic data generation for ANN training.

To evaluate the performance of the proposed method, we compare it with three widely used algorithms: the original RBFNN, the total variation (TV), and the Gauss-Newton (GN) method. Below is a brief description of each algorithm:

The original method is a neural network model that uses radial basis functions as activation units to approximate complex nonlinear mappings between input and output data. In the context of EIT, it models the relationship between boundary voltage measurements and the internal conductivity distribution. Typically, the centers of the radial basis functions are determined using clustering techniques, while their widths are calculated based on the distance between the centers. The RBFNN is known for its ability to effectively handle nonlinearities and generalize across different datasets, making it a strong candidate for image reconstruction tasks [12].

Total variation, a well-established technique for solving inverse problems such as EIT, is particularly effective in preserving edges and reducing noise. It aims to minimize the TV of the reconstructed image, promoting piecewise constant solutions. This unique feature makes it ideal for improving spatial resolution in EIT images. TV regularization solves a constrained optimization problem that balances the data fidelity and regularization terms and provides a robust solution for ill-posed problems [18].

The GN method, a widely used iterative optimization algorithm for nonlinear least-squares problems, is particularly effective in solving the inverse problem in EIT. The forward model is linearized and the difference between the measured and predicted boundary voltages is minimized. At each iteration, a linear approximation of the problem is solved to update the conductivity estimate. However, the GN method is known for its computational intensity and sensitivity to noise in the data, which can potentially affect the reconstruction quality [19].

The proposed method, which is based on a cascaded RBFNN, uses DBSCAN to calculate the centers and KNN to determine the widths of the radial basis functions, providing substantial benefits for image reconstruction in EIT. By

effectively capturing the nonlinear relationships between boundary measurements and internal conductivity distributions, this approach increases spatial resolution and improves robustness to noise. The localized nature of RBFs, combined with faster convergence and a simplified training process, facilitates real-time applications. In addition, the ability of the method to effectively generalize and interpolate missing data further improves reconstruction accuracy, making it a highly efficient and accurate solution for EIT image reconstruction. The implementation begins with DBSCAN, which clusters the input data and determines the centers of the radial basis functions. KNN is then used to calculate the appropriate widths for these functions. Finally, the optimized cascaded RBFNN is used to map the boundary measurements to the internal conductivity distribution to complete the image reconstruction task. This cascaded structure improves the ability of the method to capture complex, nonlinear relationships and provides improved accuracy and robustness in the reconstruction process, resulting in an accurate solution for image reconstruction. The algorithm proposed in Fig. 4 comprises two subnetworks:

1. The first subnetwork, which is suitable for regression and classification tasks, uses an RBFNN with explicit control of the architecture, where the DBSCAN and KNN algorithms are used to calculate the center and width of the radial basis function (RBF). These algorithms play an essential role in determining the optimal center and width of the RBF, thus improving network performance and adaptability.
2. The second subnetwork developed for generalized regression also uses an RBFNN, which is known for its simplicity and non-parametric nature. This enables it to approximate continuous functions and predict numerical values with a dynamically determined hidden layer width.

This dual-subnetwork approach leverages the strengths and adaptability of the RBFNN for robust, adaptable, data-driven modeling suitable for a wide range of problem domains.

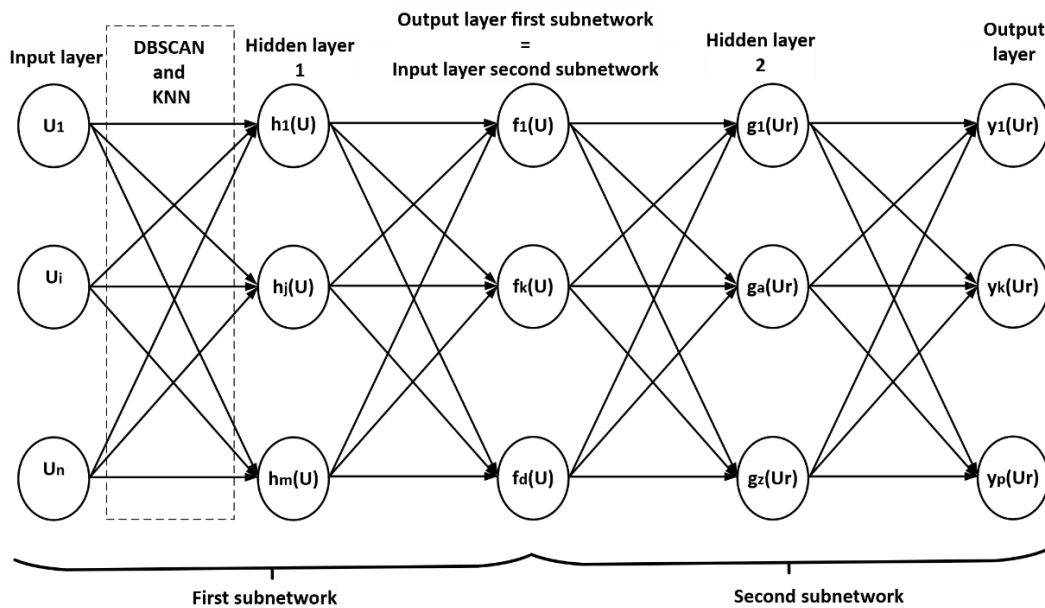


Fig. 4. Architecture of the proposed method.

DBSCAN is a clustering algorithm used in data analysis and machine learning to recognize clusters of different shapes and sizes and efficiently manage noise. It classifies points as core points that have a minimum number of neighbors within a specified radius, and then expands the clusters from these core points by iteratively collecting density-reachable points. We refer to points that are not reachable from any core point as noise. DBSCAN does not need to specify the number of clusters in advance and is therefore more flexible than other algorithms. However, the KNN algorithm is used for both classification and regression tasks. It identifies the k -nearest data points for a given input in the feature space and makes predictions based on these neighbors. In classification, KNN assigns the most common class among the neighbors, while in regression their values are averaged. The KNN algorithm is non-parametric, makes no assumptions about the data distribution, and is versatile in various applications.

The first subnetwork of the input layer in our novel algorithm comprises 208 neurons. Each input neuron processes a voltage measured according to (1). The hidden layer 1 consists of radial neurons whose centers and widths are determined by DBSCAN and KNN algorithms, respectively.

DBSCAN, a density-based clustering algorithm, identifies clusters within the data to determine the centers c_j of the RBF neurons in the first subnetwork. The cluster assignment $Cluster(u_i)$ for each point u_i is determined as follows:

$$Cluster(u_i) \begin{cases} c_1 & \text{if } u_i \text{ is a core point in cluster } c_1 \\ c_2 & \text{if } u_i \text{ is a core point in cluster } c_2 \\ \dots & \dots \\ \text{Noise} & \text{if } u_i \text{ is a core point in cluster noise} \end{cases} \quad i = 1 \dots 208. \quad (4)$$

The Euclidean distance $dist(u_i, c_i)$ between each data point u_i and the center c_i is calculated according to (5).

$$distance(u_i, c_i) = dist(u_i, c_i); \quad i = 1 \dots 208. \quad (5)$$

The KNN algorithm is then used to determine the width of the RBF neurons. The mathematical expression for identifying the nearest neighbors of u_i among the core points is given by:

$$NearestNeighbors(u_i) = \{c_1, c_2, \dots, c_k\}. \quad (6)$$

The width sp of the RBF neurons is determined using (7):

$$sp(u_i) = \max(dist(u_i, c_1), dist(u_i, c_2), \dots, dist(u_i, c_k)). \quad (7)$$

The radial neurons in the hidden layer 1 of the first subnetwork are activated according to (8):

$$h(u_i) = \exp\left(-\|u_i - c_i\|^2 * \left(\frac{1}{sp(u_i)}\right)\right); \quad i = 1 \dots 208. \quad (8)$$

where $\|u_i - c_i\|$ represents the Euclidean distance from the input vector u_i to the center vector c_i . The output of the first subnetwork $f(u_i)$ is calculated as follows:

$$f(u_i) = W_j * g(u_i) + b; \quad i = 1 \dots 208; \\ j = 1 \dots \text{maximum number of output vectors}, \quad (9)$$

where W_j is the weight assigned to the j^{th} RBF neuron and b is the bias term.

During the training process, we initialize the neural subnetwork architecture with an empty RBF layer and simulate the subnetwork. The input vector with the highest prediction error is identified and a new RBF neuron with weights initialized to this vector is added to the subnetwork. We then adjust the weights of the linear output layer using a learning algorithm to minimize the errors. This iterative process continues until the mean square error (MSE) falls below a specified target.

The output vector of the first subnetwork serves as input for the second subnetwork and consists of 1024 elements, as defined in (10):

$$ur = (ur_1, ur_2, \dots, ur_k) \quad \text{with } k = 1, 2, \dots, 1024. \quad (10)$$

The hidden layer 2 of the second subnetwork contains radial basis neurons that are activated with the Gaussian radial basis function described by (11):

$$g(ur_i) = \exp\left(-\|ur_i - cr_i\|^2 * \left(\frac{\sqrt{0.5}}{s_1}\right)\right); \quad i = 1 \dots 1024. \quad (11)$$

The activation of the RBF neuron, denoted as $g(ur_i)$, depends on the input vector ur_i . Throughout the training process, we define the center vector of the RBF as cr_i and the width parameter s_1 . The Euclidean distance $\|ur_i - cr_i\|$ quantifies the distance between the input vector ur_i and the center vector cr_i .

The output of the second subnetwork $y(ur_i)$ is a linear combination of the activations of the RBF neuron, weighted by the output weights W_j :

$$y(ur_i) = W_j * g(ur_i); \quad i = 1 \dots 1024; \quad j = 1 \dots 1024. \quad (12)$$

We calculate the mean square error (MSE) of the proposed algorithm using (13), where T_i is the target value, Y_i is the network prediction, M is the total number of responses in Y , and N is the total number of observations in Y :

$$MSE = \frac{1}{2N} \sum_{i=1}^M (Y_i - T_i); \quad i = 1 \dots 1024. \quad (13)$$

Image reconstruction is a complex process that involves the generation of a high-quality image from a set of raw data. In this process, a comprehensive set of metrics, including correlation coefficient, structural similarity index, peak signal-to-noise ratio, and accuracy, are used to assess the quality of the reconstructed image. These metrics play a crucial role in quantitatively assessing various aspects of the fidelity and overall quality of the reconstructed image, ensuring that the final image is as close to the original as possible.

The correlation coefficient cor , which is calculated in (14), is a central component of our evaluation process. It helps us to assess the degree of correlation between the recovered image Y_{mn}^* and the original image Y_{mn} . The larger the value of the correlation coefficient, the stronger the correlation and the higher the quality of the reconstructed conductivity map. $\overline{Y_{mn}^*}$ and $\overline{Y_{mn}}$ are the mean values of the recovered image and the original image, respectively.

$$cor = \frac{\sum_m \sum_n (Y_{mn}^* - \overline{Y_{mn}^*})(Y_{mn} - \overline{Y_{mn}})}{\sqrt{(\sum_m \sum_n (Y_{mn}^* - \overline{Y_{mn}^*})^2)(\sum_m \sum_n (Y_{mn} - \overline{Y_{mn}})^2)}} \quad (14)$$

The structural similarity index $ss(x,y)$ used in (15) measures the quality of the reconstructed image. A structural similarity value equal to 1 indicates that the reconstructed image and the original image are identical. A value less than 1 indicates that the quality of the reconstructed image differs from that of the original image.

$$ss(x,y) = \frac{(2\mu_x\mu_y + c_1)(2\sigma_{xy} + c_2)}{(\mu_x^2 + \mu_y^2 + c_1)(\sigma_x^2 + \sigma_y^2 + c_2)}, \quad (15)$$

where μ_x , μ_y , σ_x , σ_y and σ_{xy} are the local means, standard deviations, and cross-covariances for images x , y . The small constants C_1 and C_2 are used to prevent division by zero when calculating the structural similarity index.

The peak signal-to-noise ratio ($psnr$) calculated using (16) is essential for the assessment of image quality. It clearly indicates the fidelity of a reconstructed image compared to the original. A higher $psnr$ indicates better image quality.

$$psnr = 10 \log(\text{peakval}^2 / \text{MSE}), \quad (16)$$

where peakval is the maximum possible pixel value of the image data type and MSE is the mean square error between the recovered image and the original image.

The accuracy acc between the number of correct predictions and the total number of predictions was determined using (17):

$$acc = \frac{1}{np} \sum \text{cond}(|ncp - tnp| \leq \text{tol}), \quad (17)$$

where ncp , tnp , and np are the number of correct predictions, the total number of predictions, and the number of predictions, respectively. The variable tol is the tolerance value used to determine whether the prediction is considered correct. The indicator function cond is evaluated as 1 if the included condition is True and as 0 if it is False.

3. RESULTS

This study presents a novel approach to image reconstruction and meticulously compares it with existing algorithms in the field, including TV, the Gauss-Newton method, and the original RBFNN. The evaluation process is comprehensive and includes different types of noise, such as white Gaussian noise, impulsive noise, and contact noise, to ensure the robustness of the new method under diverse conditions. This meticulous comparison instills confidence in the thoroughness of our research.

The ablation study, performed with optimal parameters, highlighted the individual and collective contributions of each subnetwork to the overall system performance. When trained with the training dataset, the first subnetwork achieved an MSE of 0.0046. Under the same conditions, the second subnetwork achieved an MSE of 0.0202. These results were obtained using the exact optimal values for the width of the radial basis neurons in the second subnetwork, which was

set to 0.4. This significant reduction in error emphasizes the synergistic effects achieved by integrating the predictions of the two subnetworks. Although each subnetwork has different predictive capabilities, their combined model utilizes complementary strengths to improve prediction accuracy. These results highlight the fundamental importance of considering the entire architecture of the network and optimizing the parameters for better performance.

Table 1 shows the reconstructed conductivity maps using the TV, the Gauss-Newton method, and the newly proposed method. All three methods reconstruct the conductivity maps effectively when the input data is noise-free. However, in the presence of noise, the traditional algorithms struggle to produce accurate reconstructions, while the proposed method shows superior performance even in challenging conditions.

Table 2 provides quantitative evaluation metrics for the reconstructions in Table 1, including the correlation coefficient (cor), structural similarity index (ss), and $psnr$. The proposed method consistently yields higher values for these metrics than the TV and Gauss-Newton methods, regardless of noise presence, indicating superior reconstruction quality. The only exception is position 4A, where the traditional algorithms outperform the proposed method.

Table 3 shows that both the proposed and original methods can reconstruct images from data with or without noise.

Table 4 compares the correlation coefficient, structural similarity index, and peak signal-to-noise ratio between the proposed and original methods for the reconstructions in Table 3. The proposed method outperforms the original method in all metrics when the input data is noise-free or when the noise levels are between 30 and 60 dB.

Fig. 5 summarizes the accuracy results with a tolerance of $1e-6$ and gives an insight into the performance of the proposed method under different conditions. In noise-free scenarios, the proposed method achieved an impressive accuracy of 89.54 % on the test dataset, while the training data accuracy was even higher at 90.95 %.

When evaluating the performance of the method in the presence of noise, particularly at $SNRs$ ranging from 30 to 60 dB, the proposed method maintained robust accuracy levels, ranging from 82.90 % to 89.53 % for the validation dataset and from 84.28 % to 89.55 % for the test dataset. Notably, the accuracy of the validation and test datasets for the proposed method is almost identical, demonstrating its robustness under different conditions.

In comparison, the original method achieved an accuracy of 84.31 % on the validation dataset and 85.44 % on the test dataset without noise. Under noisy conditions (30 to 60 dB), its accuracy ranged from 80.90 % to 84.30 % for the validation dataset and from 81.17 % to 85.61 % for the test dataset.

The TV method, without noise, achieved an accuracy of 83.13 % on the validation dataset and 81.54 % on the test dataset. However, its performance declined significantly in noisy environments, with accuracy ranging from 33.53 % to 43.25 % for the validation dataset and from 36.17 % to 45.15 % for the test dataset.

Table 1. Comparison of reconstructed images between the new proposed method and traditional methods.

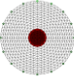
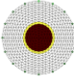
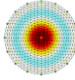
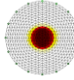
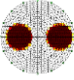
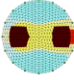
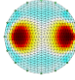
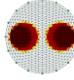
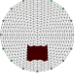
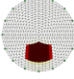
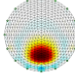
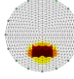
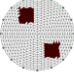
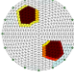
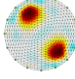
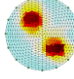
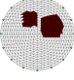
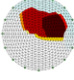
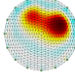
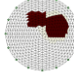

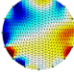
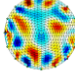
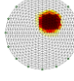

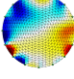
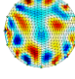
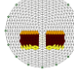
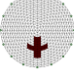
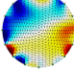
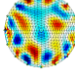
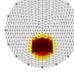
Position; Noise	Simulation model	Total variation	Gauss-Newton	Proposed method
1A				
2A				
3A				
4A				
5A				
6A; 30 dB				
7A; 40 dB				
8A; 60 dB				

Table 2. Comparison of metrics between the new proposed method and traditional methods.

Position; Noise	Metrics	Total variation	Gauss-Newton	Proposed method
1A	<i>cor</i>	0.627	0.703	0.846
	<i>ss</i>	0.964	0.929	0.978
	<i>psnr</i>	17.869	21.622	22.546
2A	<i>cor</i>	0.883	0.903	0.904
	<i>ss</i>	0.921	0.911	0.962
	<i>psnr</i>	19.231	19.114	20.327
3A	<i>cor</i>	0.836	0.831	0.867
	<i>ss</i>	0.986	0.960	0.981
	<i>psnr</i>	21.650	25.118	24.451
4A	<i>cor</i>	0.958	0.828	0.722
	<i>ss</i>	0.978	0.943	0.922
	<i>psnr</i>	23.001	23.535	20.102
5A	<i>cor</i>	0.814	0.831	0.958
	<i>ss</i>	0.955	0.925	0.995
	<i>psnr</i>	18.701	21.861	26.216
6A; 30 dB	<i>cor</i>	- 0.534	0.066	0.680
	<i>ss</i>	0.832	0.837	0.977
	<i>psnr</i>	14.057	14.912	20.918
7A; 40 dB	<i>cor</i>	0.165	- 0.087	0.691
	<i>ss</i>	0.829	0.830	0.970
	<i>psnr</i>	13.330	14.147	19.658
8A; 60 dB	<i>cor</i>	0.139	0.012	0.745
	<i>ss</i>	0.830	0.834	0.976
	<i>psnr</i>	13.429	14.815	22.142

Table 3. Comparison reconstructed images between the intelligent methods (original method and new proposed method).

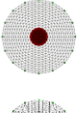
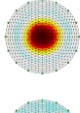
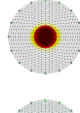
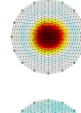
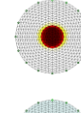
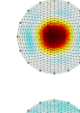
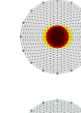
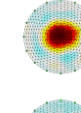
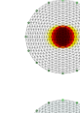
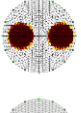
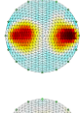
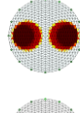
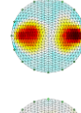
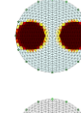
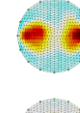
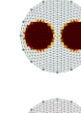
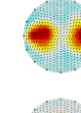
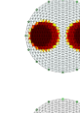
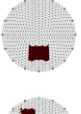
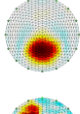
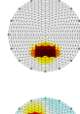
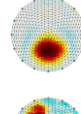
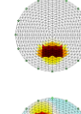
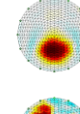
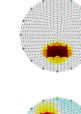
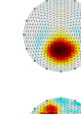
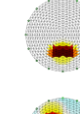
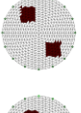
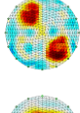
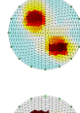
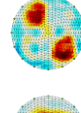
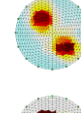
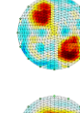
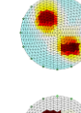
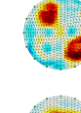
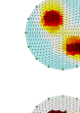
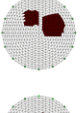
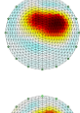
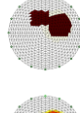
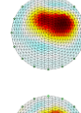
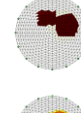
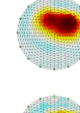
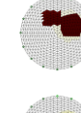
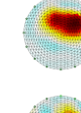
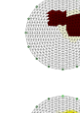
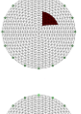
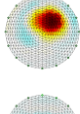
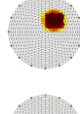
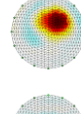
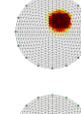
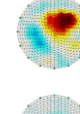
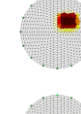
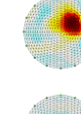
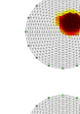

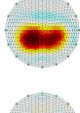
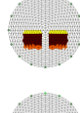
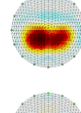
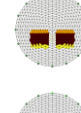
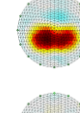
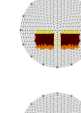
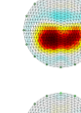
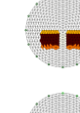
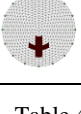
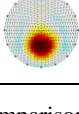
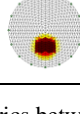
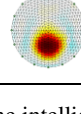
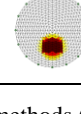
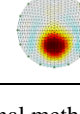
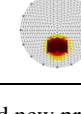
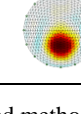
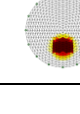
Position Noise	Simulation model	Without noise		White Gaussian noise		Non-Gaussian noise (Impulsive noise)		Non-Gaussian noise (Contact noise)	
		Original method	Proposed method	Original method	Proposed method	Original method	Proposed method	Original method	Proposed method
1B 30 dB									
2B 40 dB									
3B 50 dB									
4B 60 dB									
5B 50 dB									
6B 30 dB									
7B 40 dB									
8B 60 dB									

Table 4. Comparison metrics between the intelligent methods (original method and new proposed method).

Position Noise	Metrics	Without noise		White Gaussian noise		Non-Gaussian noise (Impulsive noise)		Non-Gaussian noise (Contact noise)	
		Original method	Proposed method	Original method	Proposed method	Original method	Proposed method	Original method	Proposed method
1B; 30 dB	<i>cor</i>	0.709	0.846	0.742	0.853	0.703	0.861	0.712	0.862
	<i>ss</i>	0.945	0.978	0.945	0.981	0.941	0.980	0.940	0.979
	<i>psnr</i>	19.414	22.546	21.087	22.532	19.683	22.856	20.183	23.392
2B; 40 dB	<i>cor</i>	0.902	0.904	0.899	0.912	0.886	0.893	0.904	0.912
	<i>ss</i>	0.913	0.962	0.905	0.954	0.902	0.957	0.912	0.962
	<i>psnr</i>	18.379	20.327	17.507	18.797	17.746	18.557	18.736	20.135
3B; 50 dB	<i>cor</i>	0.752	0.867	0.752	0.873	0.747	0.873	0.747	0.856
	<i>ss</i>	0.951	0.981	0.951	0.981	0.950	0.981	0.951	0.982
	<i>psnr</i>	21.773	24.451	21.906	24.768	21.676	24.820	21.906	24.205
4B; 60 dB	<i>cor</i>	0.663	0.722	0.663	0.722	0.663	0.722	0.663	0.723
	<i>ss</i>	0.881	0.922	0.881	0.922	0.881	0.922	0.881	0.922
	<i>psnr</i>	18.934	20.102	18.925	20.082	18.928	20.045	18.925	20.106
5B; 50 dB	<i>cor</i>	0.814	0.958	0.811	0.958	0.811	0.957	0.812	0.958
	<i>ss</i>	0.928	0.995	0.928	0.995	0.928	0.995	0.928	0.994
	<i>psnr</i>	20.979	26.216	20.875	26.212	20.881	26.208	20.875	26.208
6B; 30 dB	<i>cor</i>	0.611	0.717	0.579	0.680	0.550	0.773	0.580	0.663
	<i>ss</i>	0.943	0.978	0.928	0.977	0.913	0.983	0.932	0.970
	<i>psnr</i>	20.137	21.688	19.409	20.918	19.150	23.150	19.150	19.569
7B; 40 dB	<i>cor</i>	0.565	0.710	0.543	0.691	0.559	0.716	0.562	0.702
	<i>ss</i>	0.922	0.971	0.919	0.970	0.922	0.972	0.918	0.970
	<i>psnr</i>	18.046	19.904	17.971	19.658	18.102	20.087	18.102	19.749
8B; 60 dB	<i>cor</i>	0.674	0.745	0.674	0.745	0.674	0.745	0.674	0.746
	<i>ss</i>	0.948	0.976	0.948	0.976	0.948	0.976	0.948	0.977
	<i>psnr</i>	20.950	22.154	20.997	22.142	20.972	22.125	20.972	22.134

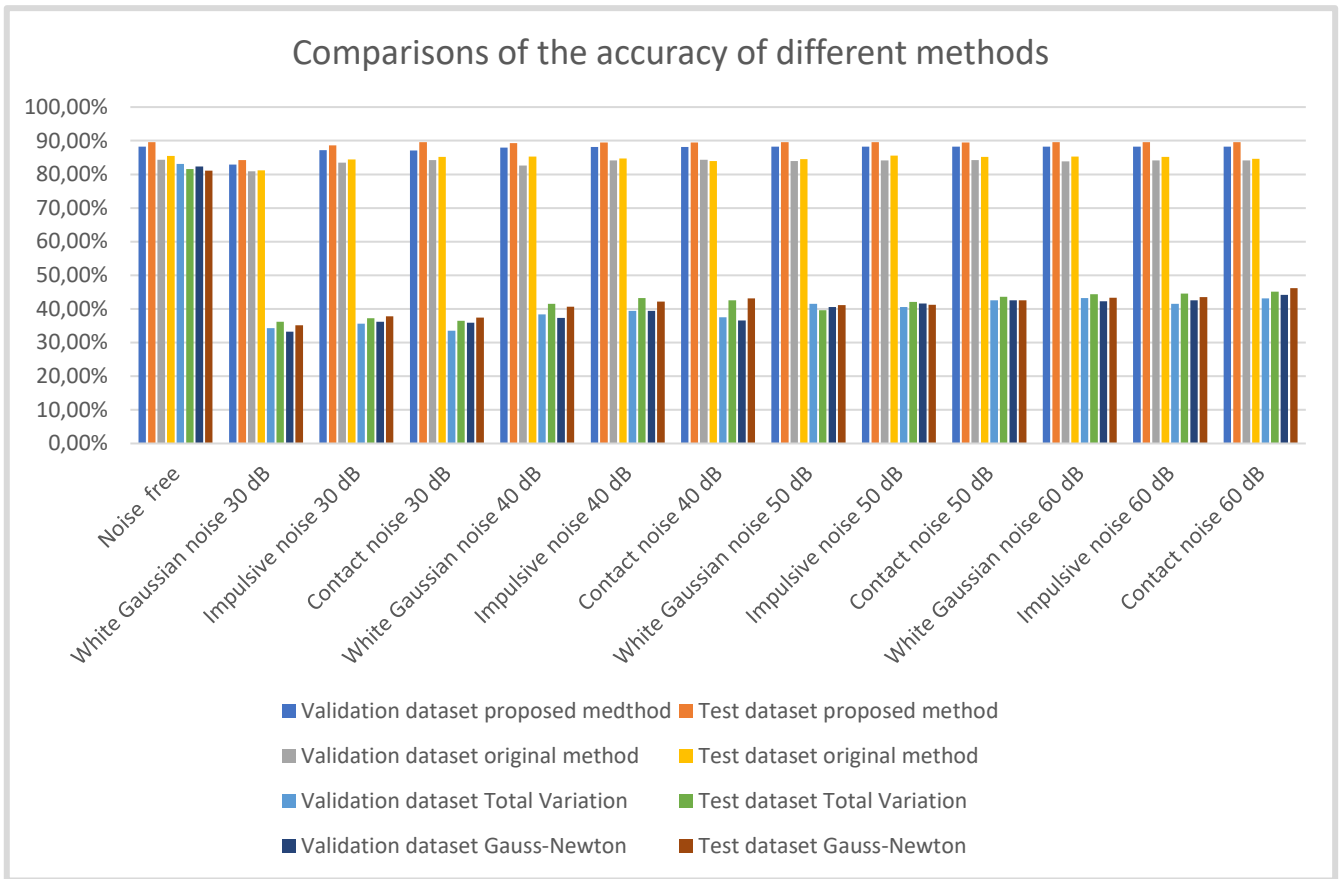


Fig 5. Accuracy comparison between the proposed method and other methods.

Similarly, the Gauss-Newton method achieved an accuracy of 82.35 % in the validation dataset and 81.14 % in the test dataset without noise. In the presence of noise, its accuracy varied between 33.21 % and 44.17 % for the validation dataset and 35.17 % and 46.15 % for the test dataset.

These results highlight the superior accuracy of the proposed method, particularly under noisy conditions, compared to the other evaluated methods.

4. DISCUSSION

The results of this study provide significant insights into the performance of the proposed method in comparison to established techniques, including TV, the Gauss-Newton method, and the original method. The proposed method shows a clear advantage over traditional approaches, especially for noisy data. It shows exceptional capabilities in reconstructing images from noisy datasets, which is a challenge that conventional methods often struggle to address. This shows that the proposed method is robust and well suited for real-world applications where data quality may be compromised.

Another notable strength of the proposed approach is its effectiveness in dealing with different types of noise, including impulsive and contact noise. This robustness emphasizes its utility in scenarios where data is inherently noisy or affected by external factors. The proposed method consistently outperforms the original algorithm even under

noise-free conditions, indicating its high effectiveness when data quality is optimal.

Specifically, the proposed method achieves an accuracy of 89.54 % without noise and maintains an accuracy between 82.90 % and 89.53 % at noise levels ranging from 30 to 60 dB. In comparison, the original method achieves an accuracy of 85.44 % without noise and an accuracy between 80.90 % and 85.31 % at similar noise levels. The TV method achieves 83.13 % without noise, with noise-influenced accuracy between 34.28 % and 45.15 %. The Gauss-Newton method has an accuracy of 82.35 % without noise, with noise-related accuracy ranging from 33.21 % to 46.15 %. These results emphasize the robustness of the proposed method, even in noisy environments.

However, the metrics of the proposed method indicate poorer reconstruction performance at position 4A in Table 2, especially for two rectangular targets. This can be attributed to the sharp edges and corners of the rectangles, which may challenge the smooth interpolation capabilities of the method. In addition, spatial interactions such as overlap, or proximity can complicate the reconstruction process when two rectangles are present. Boundary effects and sensitivity to abrupt transitions near the edges of the rectangles may also contribute to the lower performance in this region. Furthermore, while this study focused on noise levels within the range of 30 to 60 dB, we recognize the importance of evaluating the performance of the proposed method under

lower SNR conditions in future research. This will further improve our understanding of the robustness and applicability of the method in real-world scenarios where data quality may be compromised.

The promising performance of the proposed method has significant implications for a wide range of fields. Its robustness, accuracy, and adaptability make it an ideal candidate for integration into the new modular system currently under development [16]. The potential for better results with noisy or imperfect data opens up new possibilities for the application of the method.

5. CONCLUSION

In conclusion, this study shows that the proposed method significantly advances image reconstruction tasks in EIT. Its consistently superior performance, robustness to noise, and adaptability to various conditions make it a valuable tool for multiple applications.

Further research and practical implementation are crucial to fully exploit the advantages of this method and eliminate potential limitations that may occur in real-world scenarios. The integration of this approach into modular systems has the potential to significantly improve the effectiveness and reliability of EIT applications.

ACKNOWLEDGMENT

This work was supported by the internal grant agency BUT, project number FEKT-S-23-8425. We also thank the Department of Theoretical and Experimental Electrical Engineering for their valuable support.

REFERENCES

- [1] Pennati, F., Angelucci, A., Morelli, L., Bardini, S., Barzanti, E., Cavallini, F., Conelli, A., Di Federico, G., Paganelli, C., Aliverti, A. (2023). Electrical impedance tomography: From the traditional design to the novel frontier of wearables. *Sensors*, 23 (3), 1182. <https://doi.org/10.3390/s23031182>
- [2] Holder, D. (Ed.) (1993). *Clinical and Physiological Applications of Electrical Impedance Tomography*. CRC Press, ISBN 9781857281644.
- [3] Bera, T. K. (2018). Applications of electrical impedance tomography (EIT): A short review. *IOP Conference Series: Materials Science and Engineering*, 331, 012004. <https://doi.org/10.1088/1757-899X/331/1/012004>
- [4] Pessel, M., Gibert, D. (2003). Multiscale electrical impedance tomography. *Journal of Geophysical Research: Solid Earth*, 108 (B1). <https://doi.org/10.1029/2001JB000233>
- [5] Wu, Y., Hanzae, F. F., Jiang, D., Bayford, R. H., Demosthenous, A. (2021). Electrical impedance tomography for biomedical applications: Circuits and systems review. *IEEE Open Journal of Circuits and Systems*, 2, 380-397. <http://dx.doi.org/10.1109/OJCAS.2021.3075302>
- [6] Wang, H., Liu, K., Wu, Y., Wang, S., Zhang, Z., Li, F., Yao, J. (2020). Image reconstruction for electrical impedance tomography using radial basis function neural network based on hybrid particle swarm optimization algorithm. *IEEE Sensors Journal*, 21 (2), 1926-1934. <https://doi.org/10.1109/JSEN.2020.3019309>
- [7] Chen, X., Wang, Z., Zhang, X., Fu, R., Wang, D., Zhang, M., Wang, H. (2021). Deep autoencoder imaging method for electrical impedance tomography. *IEEE Transactions on Instrumentation and Measurement*, 70, 4505515. <https://doi.org/10.1109/TIM.2021.3094834>
- [8] Lin, Z., Guo, R., Zhang, K., Li, M., Fan, Y., Xu, S., Liu, D., Abubakar, A. (2022). Feature-based inversion using variational autoencoder for electrical impedance tomography. *IEEE Transactions on Instrumentation and Measurement*, 71, 4504712. <https://doi.org/10.1109/TIM.2022.3192054>
- [9] Li, X., Lu, R., Wang, Q., Wang, J., Duan, X., Sun, Y., Li, X., Zhou, Y. (2020). One-dimensional convolutional neural network (1D-CNN) image reconstruction for electrical impedance tomography. *Review of Scientific Instruments*, 91 (12), 124704. <https://doi.org/10.1063/5.0025881>
- [10] Zhang, X., Wang, Z., Fu, R., Wang, D., Chen, X., Guo, X., Wang, H. (2022). V-shaped dense denoising convolutional neural network for electrical impedance tomography. *IEEE Transactions on Instrumentation and Measurement*, 71, 4503014. <https://doi.org/10.1109/TIM.2022.3166177>
- [11] Ren, S., Guan, R., Liang, G., Dong, F. (2021). RCRC: A deep neural network for dynamic image reconstruction of electrical impedance tomography. *IEEE Transactions on Instrumentation and Measurement*, 70, 4505311. <https://doi.org/10.1109/TIM.2021.3092061>
- [12] Zhu, Z., Li, G., Luo, M., Zhang, P., Gao, Z. (2023). Electrical impedance tomography of industrial two-phase flow based on radial basis function neural network optimized by the artificial bee colony algorithm. *Sensors*, 23 (17), 7645. <https://doi.org/10.3390/s23177645>
- [13] Dong, Q., Zhang, Y., He, Q., Xu, C., Pan, X. (2023). Image reconstruction method for electrical impedance tomography based on RBF and attention mechanism. *Computers and Electrical Engineering*, 110, 108826. <https://doi.org/10.1016/j.compeleceng.2023.108826>
- [14] Wu, Y., Chen, B., Liu, K., Zhu, C., Pan, H., Jia, J. (2021). Shape reconstruction with multiphase conductivity for electrical impedance tomography using improved convolutional neural network method. *IEEE Sensors Journal*, 21 (7), 9277-9287. <https://doi.org/10.1109/JSEN.2021.3050845>

- [15] Deng, D. (2020). DBSCAN clustering algorithm based on density. In *2020 7th International Forum on Electrical Engineering and Automation (IFEEA)*. IEEE. <https://doi.org/10.1109/IFEEA51475.2020.00199>
- [16] Mikulka, J., Zimniok, D., Dušek, J. (2023). Laboratory system of electrical impedance tomography. In *2023 14th International Conference on Measurement*. IEEE. <https://doi.org/10.23919/MEASUREMENT59122.2023.10164432>
- [17] Adler, A., Boyle, A., Crabb, M. G., Grychtol, B., Lionheart, W. R. B., Tregidgo, H. F. J., Yerworth, R. (2017). EIDORS Version 3.9. In *Proceedings of the 18th International Conference on Biomedical Applications of Electrical Impedance Tomography (EIT)*. Hanover, New Hampshire, US: Thayer School of Engineering at Dartmouth.
- [18] Zhou, Z., Sato dos Santos, G., Dowrick, T., Avery, J., Sun, Z., Xu, H., Holder, D. S. (2015). Comparison of total variation algorithms for electrical impedance tomography. *Physiological Measurement*, 36 (6), 1193. <https://doi.org/10.1088/0967-3334/36/6/1193>
- [19] Islam, M. R., Kiber, M. A. (2014). Electrical impedance tomography imaging using Gauss-Newton algorithm. In *2014 International Conference on Informatics, Electronics & Vision (ICIEV)*. IEEE. <https://doi.org/10.1109/ICIEV.2014.6850719>

Received July 26, 2024
Accepted November 6, 2024